Origins of the UV/X-ray Relation in Arakelian 120

Ra'Ad David Mahmoud, Chris Done, Delphine Porquet, Andrew Lobban

To cite this version:

Ra'Ad David Mahmoud, Chris Done, Delphine Porquet, Andrew Lobban. Origins of the UV/X-ray Relation in Arakelian 120. Monthly Notices of the Royal Astronomical Society, 2023, 521 (3), pp.3585-3596. 10.1093/mnras/stac3809 . hal-03727189

HAL Id: hal-03727189
https://hal.science/hal-03727189

Submitted on 24 May 2024

Monthly Notices
of the
ROYAL ASTRONOMICAL SOCIETY

MNRAS **521,** 3585–3596 (2023) https://doi.org/10.1093/mnras/stac3809
Advance Access publication 2022 February 22

Origins of the UV/X-ray relation in Arakelian 120

R. D. Mahmoud,[1★] C. Done,[1★] D. Porquet[2] and A. Lobban[3]

[1]*Centre for Extragalactic Astronomy, Department of Physics, University of Durham, South Road, Durham DH1 3LE, UK*
[2]*Aix-Marseille University, CNRS, CNES, LAM, 13013 Marseille, France*
[3]*Astrophysics Group, School of Physical and Geographical Sciences, Keele University, Keele, Staffordshire ST5 5BG, UK*

Accepted 2022 December 22. Received 2022 November 30; in original form 2022 June 27

ABSTRACT

We explore the accretion geometry in Arakelian 120 using intensive UV and X-ray monitoring from *Swift*. The hard X-rays (1–10 keV) show large amplitude, fast (few-day) variability, so we expect reverberation from the disc to produce UV variability from the varying hard X-ray illumination. We model the spectral energy distribution (SED) including an outer standard disc (optical), an intermediate warm-Comptonization region (UV and soft X-ray), and a hot corona (hard X-rays). Unlike the lower Eddington fraction AGN (NGC 4151 and NGC 5548 at $L/L_{Edd} \sim 0.02$ and 0.03, respectively), the SED of Akn 120 ($L \sim 0.05L_{Edd}$) is dominated by the UV, restricting the impact of reverberating hard X-rays by energetics alone. Illumination from a hard X-ray corona with height $\sim 10\, R_g$ produces minimal UV variability. Increasing the coronal scale height to $\sim 100\, R_g$ improves the match to the observed amplitude of UV variability as the disc subtends a larger solid angle, but results in too much fast variability to match the UV data. The soft X-rays (connected to the UV in the warm-Comptonization model) are more variable than the hard, but again contain too much fast variability to match the observed smoother variability seen in the UV. Results on lower Eddington fraction AGN have emphasized the contribution from reverberation from larger scales (the broad-line region), but reverberation induces lags on similar time-scales to the smoothing, producing a larger delay than is compatible with the data. We conclude that the majority of the UV variability is therefore intrinsic, connected to mass-accretion rate fluctuations in the warm-Comptonization region.

Key words: accretion, accretion discs – black hole physics – galaxies: active – galaxies: individual: Ark 120.

1 INTRODUCTION

The emission from Active Galaxies Nuclei (AGN) and Quasars is typically variable even in radio-quiet (non-jet dominated) objects, with the fastest time-scales seen at X-ray energies. Light travel time sets a minimum size scale, and it was this, coupled to the large luminosities, which led to the first identification of the central object with an accreting supermassive black hole.

The origin of the X-ray emission in AGN is not well understood. Standard disc models predict a maximum disc temperature which is too low to produce much X-ray flux, peaking instead in the (unobservable) far ultraviolet (FUV)/extreme ultraviolet (EUV) for most masses, spins and accretion rates. Nonetheless, stellar-mass accreting black holes in our Galaxy also produce X-ray emission at energies above their disc peak, where it is generally assumed to be produced by hot, optically thin plasma which is either above an optically thick disc (sandwich corona), or is on the spin axis of the black hole (lamppost) or replaces the disc in the inner regions (truncated disc/hot-inner flow). Additionally in AGN (and also in some of the more complex spectra seen from stellar-mass black holes) there is another spectral component which spans between the disc and hot corona. In AGN this is typically seen as a ‘soft X-ray excess’. a rise in the spectrum above the low-energy extrapolation of the power-law spectrum seen in 2–10 keV. This can be well fit by warm, optically thick Comptonization (Porquet et al. 2004; Gierliński & Done 2004a), or alternatively by extremely strong relativistically smeared reflection of the power law from the disc (Crummy at al. 2006). Some fraction of the soft X-rays reverberate, so must be from reprocessing as they follow the variability of the hard X-ray power law but with a lag (e.g. Kara et al. 2013; Uttley et al. 2014). However, the majority of the soft X-ray excess is now thought to be a true additional component (Mehdipour et al. 2011, 2015; Matt et al. 2014; Boissay, Ricci & Paltani 2016; Petrucci et al. 2018; Porquet et al. 2021).

Going further down in energy, the spectrum which emerges from interstellar absorption in the UV is often very blue, but not as blue as expected from the outer radii of a standard accretion disc. Pure disc models have $F_\nu \propto \nu^{1/3}$, while average near UV spectral slopes (from SDSS spectra for $0.7 < z < 1.1$) are $F_\nu \propto \nu^{-1/3}$ (Xie, Li & Hao 2016; Davis, Woo & Blaes 2007). Some part of this may be due reddening from dust local to the AGN environment, but these redder slopes are clearly intrinsic in some AGN, and this UV downturn can connect to the warm-Comptonization models for the soft X-ray excess (e.g. Mehdipour et al. 2011; Done et al. 2012; Jin et al. 2012; Matt et al. 2014; Petrucci et al. 2018; Kubota & Done 2018).

These spectral observations can be tied together to inform a potential structure for the accretion flow, where the emission thermalizes as in a standard disc only in the outer regions. Inwards of some radius, R_{warm}, thermalization is incomplete, so the disc emits as warm

---

★ E-mail: mahmoud.raad@yahoo.co.uk (RDM); chris.done@durham.ac.uk (CD)

Published by Oxford University Press on behalf of Royal Astronomical Society

Comptonization rather than blackbody flux. Then at $R = R_{hot}$, the disc disappears completely, being replaced by a hot-inner flow (Done et al. 2012; Kubota & Done 2018).

This three-component approach can also explain the observed trends in spectral shape with mass accretion rate (scaled to the Eddington luminosity, hereafter L/L_{Edd}) with a single additional assumption that the hot corona always has $L/L_{Edd} = 0.02$, which is the maximal luminosity for an advection dominated accretion flow (Kubota & Done 2018). This sets the radius, R_{hot}, within which all the gravitational energy of the flow needs to be dissipated in heating the hot plasma. For AGN with $L_{bol}/L_{Edd} < 0.02$, the entire inner disc is replaced by a hot flow. The lack of a strong UV emitting inner disc means that the UV flux illuminating the broad-line region (BLR) is much reduced, so the broad permitted line signature of AGN activity is likewise much less evident. This can explain the abrupt transition of 'changing state' AGN, where the UV drops abruptly below $L/L_{Edd} = 0.02$, in a very similar manner to the abrupt drop in disc flux in the stellar-mass black hole binaries as they dim below this luminosity (Noda & Done 2018; Ruan et al. 2019). Above $L_{bol}/L_{Edd} \sim 0.02$ there is some residual UV emission from the outer disc/warm-Compton disc, but the majority of the accretion energy is dissipated in the inner hot flow. It is only for $L_{bol}/L_{Edd} > 0.1$–0.2 that the hot flow is less than 10 per cent of the total power. This decreasing ratio between the hot X-ray emission and the optically thick disc, (L_x/L_{UV}), with increasing L/L_{Edd} matches the quasar results of Lusso & Risaliti (2017), and also implies that there are more seed photons cooling the hot plasma, steepening the hard X-ray spectral index with increasing L/L_{Edd} as observed.

This is a specific geometry, which is testable using the intensive reverberation campaigns, where optical, UV and X-rays are monitored simultaneously with the *Swift* satellite. These large campaigns show differential lags across the UV and optical, with the FUV responding first, followed by longer wavelengths with progressively longer lags (e.g. Edelson et al. 2015, 2017, 2019). However, these lag time-scales are typically larger than expected from illumination of the outer disc by a central X-ray source, irrespective of whether the disc is somewhat truncated on its inner edge and/or covered by a warm-Compton region as expected in the radially stratified models of the accretion flow described above (Gardner & Done 2017; Mahmoud & Done 2018). The data require much larger size scales for the reprocessor if light travel time sets the lags. There is some convergence in the literature that there is an additional diffuse emission component, either from the BLR itself (Korista & Goad 2001, 2019; Lawther et al. 2018) or from a wind inwards of the BLR (Dehghanian et al. 2019; Kara et al. 2021). This is seen directly as an increased lag around the Balmer continuum (Cackett et al. 2018; Edelson et al. 2019; Cackett, Zoghbi & Otho 2022). The longer lags could also indicate the X-ray source is not central, but is instead at a much larger distance from the accretion disc, along the black hole spin axis (Kammoun, Papadakis & Dovčiak 2019, 2021). However, a more fundamental problem with both these solutions is that the UV is poorly correlated with the X-rays which are meant to be driving the whole variability (e.g. Edelson et al. 2019).

X-ray variability can be complicated. There can be spectral pivoting (a steeper power law when the spectrum is brighter) so that the bolometric flux varies differently to that in the observed (generally 2–10 keV) X-ray bandpass. There can also be absorption variability along the line of sight, which likewise means that the observed X-ray flux does not track the intrinsic variability seen by the disc. Variable X-ray absorption is particularly an issue in NGC 5548, the first AGN used for these campaigns, as it was unusually obscured during the monitoring (Mehdipour et al. 2016; Dehghanian et al. 2019). Similar issues are now clearly present in Markarian 817 (Kara et al. 2021).

Hard X-ray monitoring circumvents both these uncertainties, as it much less affected by the absorption variability. However, NGC 4151 is the only AGN which is bright enough for *Swift* BAT monitoring above 10 keV, and this showed clearly that the disc was strongly truncated, with no optically thick material responding within a few hundred R_g (Mahmoud & Done 2020, hereafter MD20). This was independently confirmed by studies of the iron line profile which is marginally resolved in Chandra HETGS (Miller et al. 2018), indicating an origin at inner BLR scales, as also supported by newer iron line reverberation studies (Zoghbi, Miller & Cackett 2019). This is consistent with the models described above, as NGC 4151 was below $L = 0.02\ L_{Edd}$ during the campaign, so should not have an inner UV bright disc. Nonetheless, there *is* a potential reprocessing signal in the UV in these data. It is instead consistent with material in the inner BLR. A reprocessed continuum component from the densest clouds in the BLR is expected theoretically (Korista & Goad 2001, 2019; Lawther et al. 2018). All sketches of the BLR have it subtending a much larger solid angle to the central source than the flat disc, and its reprocessed signal fits the time-scales seen in the reverberation data (Korista & Goad 2019).

There is another way to circumvent the uncertainties in going from observed X-ray 2–10 keV flux to bolometric, and that is to use one of the 'bare' AGN (Patrick et al. 2011; Walton et al. 2013) which (a) show no absorption in their soft X-ray spectra, so that absorption variability is not an issue, and (b) provide good enough statistics in the X-ray bandpass up to 10 keV that one can model the effects of spectral pivoting. This selects Ark 120, which spans $L/L_{Edd} \sim 0.04 - 0.06$, so according to the models above should have some outer disc/warm-Compton component to explore in reverberation (as well as the BLR/inner wind). We use the recent *Swift* UV and X-ray monitoring, combined with *XMM–Newton*/NuSTAR data to determine the spectral components and their variability, and use this to determine limits on the accretion geometry at this brighter L/L_{Edd}.

2 DATA

We need both good quality spectra and good quality light curves to build a spectral-timing model where the reprocessed variability in optical and UV can be predicted from the observed X-ray flux. We choose the combination of XMM-NuSTAR spectra from 2013 February 18 to 2014 March 22, and *Swift* XRT-UVOT monitoring data covering a ~6-month period, from 2014 September 04 to 2015 March 15 (Porquet et al. 2018, hereafter P18; Lobban et al. 2018, hereafter L18, see also Gliozzi et al. 2017, Buisson et al. 2017). While the XMM-NuSTAR snapshots do not overlap in time with the *Swift* monitoring, the lowest and highest points on the X-ray light curves in the *Swift* monitoring match the X-ray flux from the 2013 (low) and 2014 (high) XMM-NuSTAR spectra (P18, L18) so we use these to define the spectral range.

2.1 *Swift* light curves

There are a total of 86 *Swift* observations in the 2014 campaign (ObsID: 00091909XXX), each separated by ~2 d, with typical duration of ~1 ks. The U and UVM2 filters were alternated, so each UV filter point has typical separation of ~4 d (L18). We choose to focus on the shortest wavelength band, UVM2, as this is least affected by host galaxy and BLR contamination.

Fig. 1 shows the mean-normalized X-ray and UVM2 light curves. The XRT data are split into two energy bands, the hard X-rays from

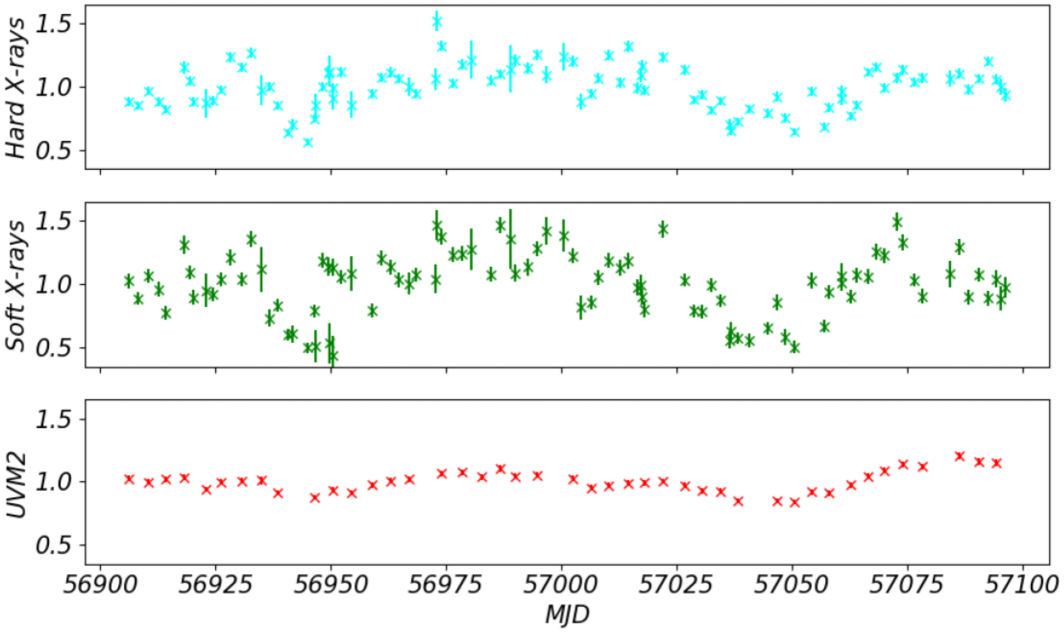

Figure 1. The raw, mean-normalized light curves for this campaign in the bandpasses of the HX (1–10 keV, uppermost panel), SX (0.3–1 keV, middle panel), and UVM2 (lower panel).

1–10 keV (hereafter HX) and soft X-rays from 0.3–1 keV (hereafter SX), from L18. Each data set has been normalized to its mean count rate, showing clearly that there is more variability on these time-scales in HX and SX than in UVM2, but that the light curves are fairly well correlated by eye on these time-scales. The error-subtracted HX variance is 0.174, while the SX variance is larger, at 0.250. This already presents a challenge for models where all variability is reprocessed HX flux, although it could perhaps be produced by temperature variability of the warm Comptonization amplifying the response over a small SX band.

2.2 ARK 120 spectral energy distribution (SED)

The XMM-NuSTAR observations from P18, which includes XMM-OM UV data, gives the full SED at two epochs. We fit the spectra from these two epochs jointly in `XSPEC`. To do this, we follow MD20 by applying the `agnsed` model of Kubota & Done (2018), which consists of an outer standard disc (red lines), a warm-Comptonized disc (green lines), and (blue) hard-Compton components. In addition to this, we include neutral reflection using `pexmon`, relativistically smoothed with `rdblur` representing mildly blurred-disc reflection (N16, P18, and P19). The more detailed spectral study in P18 uses the more sophisticated `relxill` reflection models, but their best fit is only mildly ionized so the simpler neutral reflection model is appropriate for our purpose which is simply to extract the underlying continuum. We also include a free narrow Gaussian component to model the ionized emission line seen at 6.95 keV, and one to match the slightly broadened 6.4 keV line which is likely from the BLR/inner wind (P18). The total model is absorbed by the interstellar medium using `tbfeo` (Wilms, Allen & McCray 2000) for gas and `redden` (Cardelli, Clayton & Mathis 1989) for dust so the total model is `constant * tbfeo * redden * (rdblur * pexmon + agnsed + zgauss + zgauss)`. The assumed geometry for the `agnsed` model is shown in Fig. 2(a). It is noteworthy that this model assumes a real truncation of the optically thick disc at R_{hot}, so predicts an iron line from disc reflection which is not highly relativistically smeared. This is consistent with more detailed reflection spectral fits to the data, as discussed in P18.

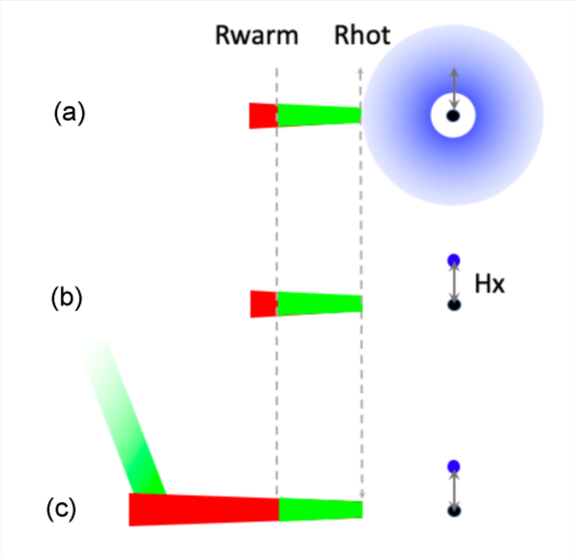

Figure 2. The geometries assumed in this paper (a) the intrinsic components of the `agnsed` model, (b) the extended HX Comptonizing region is assumed to be a point source at height H_x above the black hole on the spin axis for ease of calculation of the reprocessed emission, and (c) includes the additional reprocessor connected to the inner BLR and/or its wind.

The `agnsed` model also includes the reprocessed HX emission. Gardner & Done (2017) show explicitly that an extended HX source with emissivity like that expected from a thin disc gives an illumination pattern that is extremely similar to that from a much simpler point source at height $H_x = 10\ R_g$ above the spin axis (Fig. 2b).

Fig. 3 shows the observed data and unabsorbed model fit lines from the high epoch (black circles, dashed lines) and low epoch

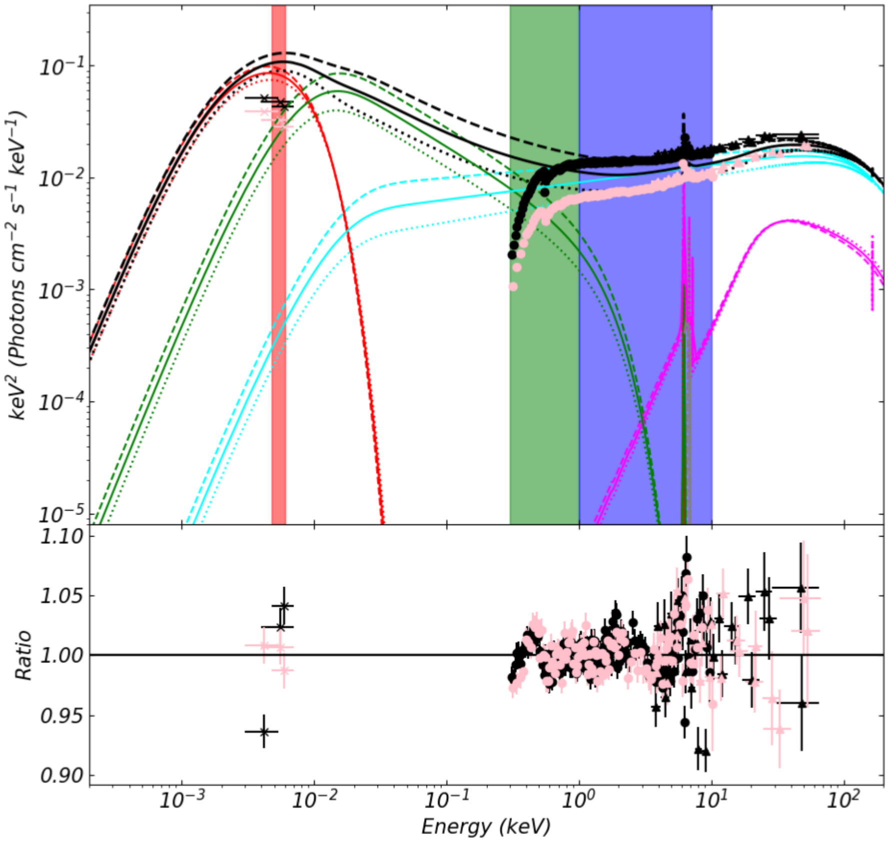

Figure 3. Top panel: broad-band spectrum and SED for the XMM-NuSTAR observations of P18. The red vertical line indicates the UVM2 band, while the green and blue show the SX and HX bands. The black points show the observed (i.e. absorbed) high-luminosity (2014) epoch. The pale pink points are the low-luminosity (2013) epoch (absorbed). The (unabsorbed) best-fit model to the 2014 observations is shown as the black-dashed line with components in dashed red (SS disk), dashed green (soft Compton), and dashed turquoise (hard Compton). The (unabsorbed) best-fit model to the 2013 observations is shown as the dotted black line with components in dotted red (SS disk), dotted green (soft Compton), and dotted turquoise (hard Compton). The average spectrum between the two epochs is shown as the solid-black line, with solid components (colours correspond to the same as individual epochs, above). We take this spectrum to be the assumed mean spectrum during the *Swift* monitoring campaign. Relativistic reflection and the free Gaussian lines are also shown in pink and grey respectively, where the line styles denote each epoch and the mean as above. Bottom panel: residual ratios of the high- and low-luminosity epoch data to their best-fit spectral models (when absorption is applied).

(pink circles, dotted lines). These are well fit, as shown by the lower residual panel, and give a total Eddington fraction of $L/L_{Edd} =$ 6.3 per cent and 3.8 per cent for the higher and lower luminosity epochs respectively for this black hole mass of $1.5 \times 10^8\, M_{\odot}$, so both mass and mass accretion rate are slightly higher than in NGC 5548, and the SED has higher UV to X-ray luminosity showing there is some intrinsic inner disc emission (see also Kubota & Done 2018).

To infer the light-curve contributions from each component, we would like the mean SED during the monitoring campaign period. Fortunately, the fluxes in each of the high and low epochs match the high- and low-flux limits during the monitoring campaign period from 2014 to 2015. We can therefore take the mean SED during the monitoring campaign period to be the spectrum bisecting the higher and lower luminosity epochs. This intermediate spectrum is shown as the solid lines in Fig. 3.

3 LIGHT CURVES OF THE COMPONENTS

The spectral index of the HX clearly varies with flux, softening as the source brightens (L18), but peaking always at high energies, above 50 keV. Thus the bolometric HX coronal flux varies by less than the 1–10 keV flux. We reconstruct the bolometric HX variability by using the observed spectral pivoting between the 2013 and 2014 spectra, and interpolating between them, assuming that there is a one-to-one relation between 1–10 keV flux and spectral index (as is generally seen: Lobban et al. 2020), and assuming that the electron temperature stays constant at 100 keV.

The top panel of Fig. 4 shows the observed mean normalized 1–10 keV light curve (cyan crosses) together with the inferred mean-normalized bolometric variability (dark-blue dashed). The two are extremely similar, as this correction is only of order 10 per cent. We also use the inferred index and normalization to extrapolate the hot-corona spectrum down, and find that the hot-Compton component produces 63 per cent of the flux in the SX band. We subtract the hard variability, scaled by this proportion, from the observed 0.3–1 keV flux so as to separate the variability of the SX excess component from the underlying variability of the hot corona. This correction has a larger effect. The light green crosses in the middle panel of Fig. 4 show the normalized total 0.3–1 keV light curve which includes both the hot-corona variability and the soft excess, while the dark green shows the new estimate of the variability of the SX excess alone. This now has noticeably more variability, increasing the tension noted earlier. There must be intrinsic variability in the SX excess on these time-scales, as is seen even more clearly by comparing the two SX

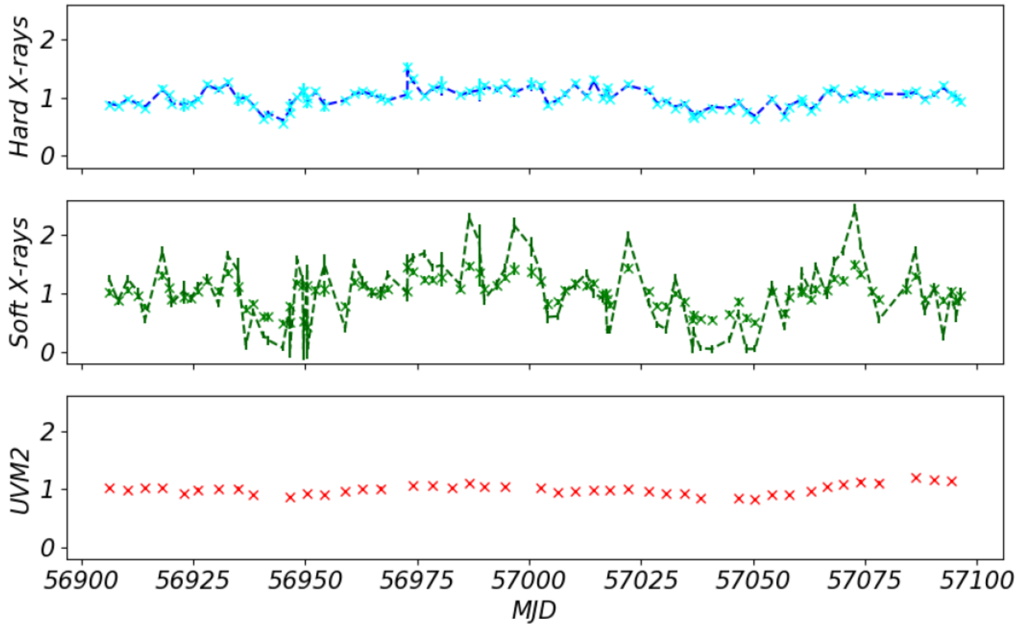

Figure 4. Crosses are the observed light curves in the HX, SX, and UVM2 bands, as in Fig. 1. The cyan-dashed line shows the inferred mean-normalized variations of the hard-Compton component at its bolometric peak, where the variation amplitudes are adjusted for the expected pivoting and higher mean. The green-dashed line denotes the expected variations in the SX component, assuming the non-pivoting case. This is inferred from the soft-band light curve, by computing how the hard component contribution in the soft band are expected to vary, subtracting these variations from the observed soft-band curve, and mean-normalizing the resultant curve. We see that the SX component is intrinsically more variable than the soft-band curve itself.

components in the SED fitting in Section 2.2 (see also fig. 1 in P18), where the total luminosity of the warm-Comptonized component changes by a factor of 2.2 between 2014 and 2013, while that of the hot Comptonization changes by only a factor 1.7. The modelled change in warm Comptonization normalization cannot therefore be driven by reprocessing of the hot component in a constant geometry.

We use the mean of the inferred bolometric HX variability to derive the mean HX Compton component in Fig. 3. We then compute the variable reprocessing resulting from this component as it illuminates the warm-Compton region and outer standard disc, assuming that these are intrinsically constant. To do this, we closely follow the timing simulation procedure of MD20, whereby the seed photon temperature at each disc annulus is modulated according to the reprocessed flux variations as

$$T_{seed}(r,\ t) = T_{grav}(r)\left(\frac{F_{rep}(r,\ t) + F_{grav}(r)}{F_{grav}(r)}\right)^{1/4}, \qquad (1)$$

where T_{grav} and F_{grav} are the local temperature and energy flux due to gravitational dissipation, and F_{rep} is the flux incident on the local annulus from the hard-Compton source. The only difference in our procedure for Ark 120 is that we now include flux variations in outer thermal disc as well as the warm-Compton disc, since the thermal disc component contributes significantly to the UV bandpass according to the Ark 120 SED. This is unlike NGC 4151, where the disc component was too cool to contribute to the UV. The difference in extent of the disc is as expected for the difference in L/L_{Edd} between these two objects.

The inferred bolometric X-ray light curve has the same sampling as the observed X-ray light curve, of around 2 d, while the alternating UV filters mean that the UV sampling interval in any single band is around 4 d. Each observation length is only 1 ks, so the data are sampled rather than binned. Plainly this could mean that some of the fast X-ray variability is missed as the power spectrum of the 1–10 keV light curve is consistent with a power law, with $PSD(f) \propto f^{-2}$ down to time-scales below 1000 s (see e.g. fig. 12 in L18). We therefore use the continuous-time autoregressive moving average (CARMA) model of Kelly et al. (2014) to simulate the range of variability which might be missed by the gaps in the sampled X-ray light curve. We then reprocess this range of possible full light curves from the warm Compton and outer standard disc to give the predicted UVM2 reprocessed signal in each of the models below.

Fig. 5 shows the autocorrelation functions (ACFs) of the light curves in each band. The top panel shows the ACFs of each raw light curve as solid lines, with U (red) and UVM2 (black) clearly broader than the SX (light-green solid) and HX (light-blue solid). The ACF of the reconstructed hard-Compton component (dashed dark blue) lies almost completely on top of the raw HX count rate, as it is approximately a scaled version of the observed HX variability. However, the ACF of the reconstructed SX Compton component variability (dark-green dashed line) is somewhat different in shape to the SX count rate curve (solid pale green line) due to the removal of the HX variability in this band.

The CCFs of each observed light curve against UVM2 is shown in the middle panel. The U band (red) is extremely well correlated with UVM2 ($CCF^{max}_{UVM2,U} = 0.98$), while the observed SX (green) and HX (blue) are not ($CCF^{max}_{UVM2,SX} = 0.67$, $CCF^{max}_{UVM2,HX} = 0.65$). The magenta line shows the cross-correlation between the observed SX and HX light curves. Clearly there is some correlation between these on short time-scales, but much of this is due to the SX light curve including some of the HX variability. The magenta line in the lower panel shows the cross-correlation of the derived SX and HX Compton components, clearly showing the drop in peak at zero lag by removing the contribution of hard Compton from the soft band. The lower panel shows the CCFs of these separated soft Compton (green) and hard Compton (blue) X-ray component variability relative to UVM2. Clearly they are not well correlated.

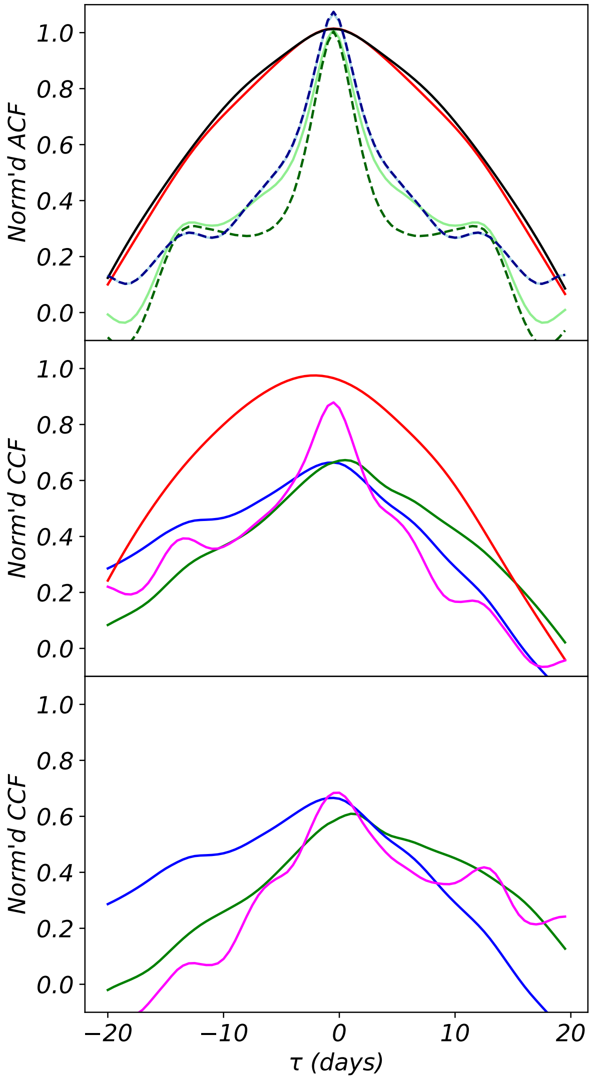

Figure 5. Top panel: ACFs for the U band (red solid), UVM2 (black solid), SX (pale-green solid), HX (pale blue solid), and derived hard Compton (blue dashed), derived soft Compton (green dashed). Middle panel: cross-correlation functions (CCFs) between UVM2 count curve and U (red solid); observed SX (light-green solid); observed HX (blue). Also the cross-correlation between the observed SX and HX count curves (magenta). Bottom panel: CCFs between the UVM2 count curve, and the derived soft-Compton curve (green); the derived hard-Compton curve (blue). Also the CCF between the derived soft- and hard-Compton curves (magenta).

4 REPROCESSING OF THE HOT COMPTON COMPONENT

Here we will introduce the first spectral-timing model of this paper. In this basic case, we assume that only the hard-Compton component (the corona) varies independently, and that all other variations are driven by reprocessing of this hard-coronal power (see the geometry in Figs 2 a and b). This is in tension with the larger variability seen in SX than in the hard, but here we are focused instead on what this standard idea of HX reprocessing produces in the UV band.

The uppermost panel of Fig. 6 shows the mean-normalized bolometric hot Comptonization component light curve. The middle panel shows the predicted (red) and observed (blue) response in UVM2. This was calculated assuming that the X-ray corona has mean height of $h_x = 10$, as in the `agnsed` fit, in order to calculate the illumination. This is a very poor match to the observed UVM2 light curve, predicting much smaller variability amplitude than is seen in the data, and an overall root-mean-square (rms) error with respect to the data of 7×10^{-2}. The grey lines in the middle panel show the UV curves predicted from 10 CARMA realizations of the X-ray input, displaying the range of UV curves predicted by this model which could have arisen due to under-sampling (clearly insufficient to match the observations, in blue).

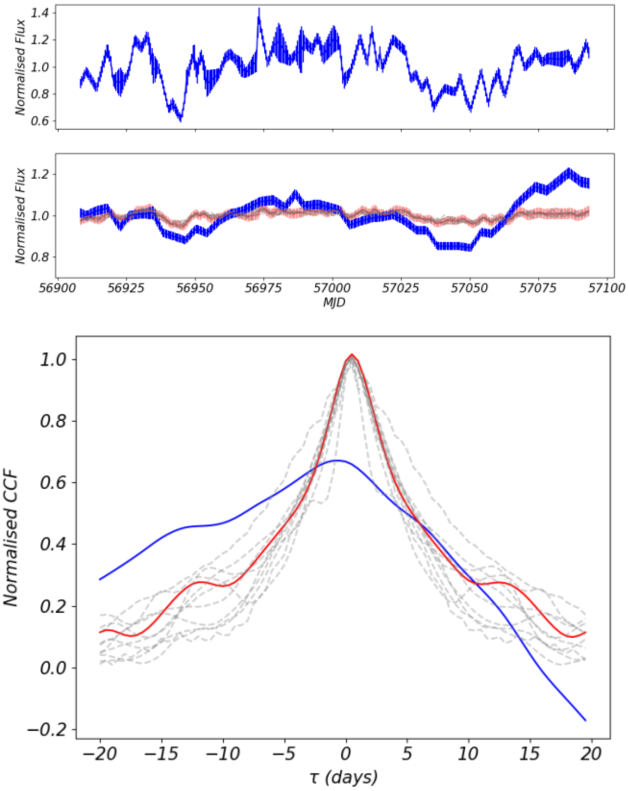

Figure 6. Results for model **HX10**. Top panel: HX light curve from *Swift*. Middle panel: disc+warm Compton reprocessing of only hard-illuminating flux, no intrinsic soft variability. Observed UVM2 light curve is shown in blue, with the model prediction in red assuming observed hard-Compton input. Grey lines show UVM2 timing model predictions with CARMA HX light-curve realizations as input. Bottom panel: CCFs for the observed (blue) and simulated (red) light curves, with model predictions based on CARMA HX light-curve realizations in grey.

The CCF of UVM2 with the HX reveals another mismatch, in that the predicted small amplitude variability is fast, and well correlated with the HX on time-scales of days, as the model UV disc size is small. It predicts a peak correlation between the fluctuations in UVM2 and HX which is close to unity, and a width of around 4 d; that is, it looks like the ACF of the HX, while the observed UVM2 cross-correlation (blue line) is much broader and weaker. This model is clearly wrong, as the true correlation corresponds to only $CCF^{max}_{UVM2,\,HX} = 0.65$. Most of the observed UV variability is not produced by HX illumination of a disc, where the UV is produced in a region ~30–100 R_g (less than 1 light-day) by a source of typical height 10 R_g.

This model, with reprocessing of the hard Compton from $h_x = 10$ in the disc and warm-Compton zones, will be referred to as **HX10**.

One way to get more response in the UV from the same X-ray flux variability is to change the geometry so that the disc subtends

Table 1. Obtained parameters for `agnsed` from fitting to the time-averaged 2013 and 2014 epoch data. 'F' denotes a fixed parameter. First and second columns denote fit using $h_x = 10$, used in most of the paper and shown explicitly in Fig. 3. Third and fourth columns denote fit using $h_x = 100$, used primarily in Fig. 7.

	$h_x = 10$ case		$h_x = 100$ case	
Observation	2013 (Low)	2014 (High)	2013 (Low)	2014 (High)
M_{BH}	1.5×10^8 (F)	= =	= =	= =
D	143.5 (F)	= =	= =	= =
a^*	0 (F)	= =	= =	= =
$\cos(i)$	1. (F)	= =	= =	= =
$\log(\dot{m})$	-1.42 ± 0.02	-1.20 ± 0.01	$-1.42^{+0.03}_{-0.02}$	-1.23 ± 0.02
$kT_{e,\,hot}$	100. (F)	= =	= =	= =
$kT_{e,\,warm}$	$0.361^{+0.002}_{-0.001}$	0.342 ± 0.002	0.366 ± 0.003	0.348 ± 0.001
Γ_{hot}	$1.80^{+0.01}_{-0.02}$	1.90 ± 0.01	$1.80^{+0.02}_{-0.03}$	$1.89^{+0.02}_{-0.01}$
Γ_{warm}	2.70 (F)	= =	= =	= =
R_{hot}	23.0 ± 0.2	$23.1^{+0.3}_{-0.2}$	23.1 ± 0.3	$22.8^{+0.1}_{-0.2}$
R_{warm}	46^{+2}_{-1}	61 ± 1	46.4 ± 0.3	63 ± 1
$\log(r_{out})$	-1 (F)	= =	= =	= =
h_{max}	10 (F)	= =	100 (F)	= =
Reprocess	1 (F)	= =	= =	= =
Redshift	0.0327 (F)	= =	= =	= =

a larger solid angle to the X-ray source. While $H_x = 10\ R_g$ is roughly the expected size scale of gravitational energy release, the hot-corona scale height could be larger and/or the corona itself could be associated with the base of a jet at some larger scale height above the black hole (see Fig. 2b). We refit the data using an X-ray scale height of $H_x = 100\ R_g$. This does give more reprocessing in the UV but this is still not a large fraction of the total UV flux as the HX bolometric power is smaller than the UV. Hence the new spectral fit with `agnsed` with height fixed to $H_x = 100\ R_g$ has all other parameters very similar to those derived from the original fits at $H_x = 10\ R_g$, and with almost identical goodness of fit ($\chi^2_\nu = 1.14$: Table 1).

The resultant UVM2 light curve is shown in Fig. 7. This again assumes only reprocessing of the hard-Compton fluctuations on the blackbody/warm-Compton disc zones, but now the amplitude is comparable to that seen in the data. However, the predicted UVM2 light curve is not a good match to the observed UVM2 variability. The predicted light curve has too much fast variability compared to the observed data.

It is clear that the disc as assumed in the $H_x = 100\ R_g$ `agnsed` model – where there is optically thick material at $R > 23\ R_g$ (though most of the response comes from $R \sim H_x = 100\ R_g = 1$ light day) – is too close to the X-ray source for light travel time delays to smooth out the observed fast X-ray fluctuations to a level compatible with the rather smooth (20 light day ACF width) UV variability.

While this model initially looked promising (see also Noda et al. 2016 on NGC 3516 where they show that this model can work with sparse sampling of the X-ray and optical light curves), this is not a good match to this data in detail, with the rms error with respect to the observations at 7×10^{-2}, similar to the $h_x = 10$ case. Further, the CCF shows explicitly that the predicted correlation on short time-scales (4 d) is much stronger than seen in the real data. Thus while a large scale height X-ray source could match the UVM2 variability amplitude, it predicts too much correlated variability on short (4 d) time-scales. This is consistent with the transfer functions shown for different scale height sources in Kammoun, Papadakis & Dovčiak (2019; their Fig. 1), where the UV response peaks below 1 ld for NGC 5548, which translates to a few light days in the higher mass, higher mass accretion rate of Akn 120.

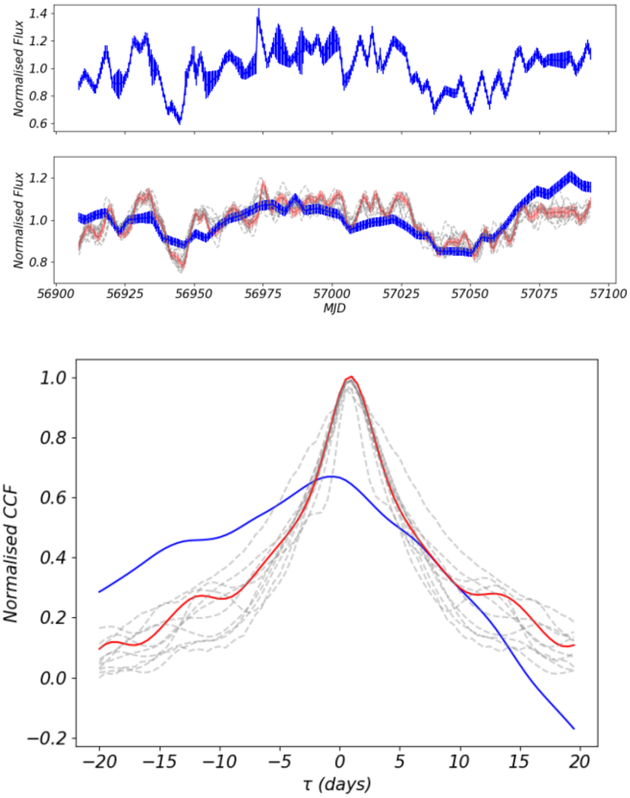

Figure 7. As in **HX10** (Fig. 6), but with the hard corona scale height set to $h_x = 100$.

The clear result of this modelling is that most of the UV variability can not arise from reprocessing of the HX on the accretion disc as this predicts too much fast variability on time-scales of a few days when matched to the detailed shape of the UV light curve rather than just the mean lags.

5 REPROCESSING OF HOT COMPTON PLUS INTRINSIC VARIABILITY OF WARM COMPTON

We now fold the additional variability – which is clearly present in the SX flux associated with the warm-Compton component – into our model. The existence of this independent variability in the SX/UV component already challenges the above picture involving only reprocessing of hard fluctuations, as does simple energetics. The total flux in the low (high) state (including reprocessing from the source at height 10 R_g) is $5.0(8.3)\times\ 10^{-10}$ ergs cm^{-2} s^{-1}, with flux in the hot Compton of $1.2(2.0)\times\ 10^{-10}$ ergs cm^{-2} s^{-1}. Thus the flux change in the HX is $0.8\ \times\ 10^{-10}$ ergs cm^{-2} s^{-1}, yet the change in the inferred optical/UV and SX components, respectively are 0.6×10^{-10} ergs cm^{-2} s^{-1} and 1.9×10^{-10} ergs cm^{-2} s^{-1}. Clearly there must be intrinsic variability in the UV, as the flux change from HX alone is insufficient to drive these variations.

The accretion models used here associate the SX component with the high-energy emission of an optically thick, warm-Comptonization region: a part of the accretion disc where thermalization is incomplete. This same component extends down to the UV in this model, so the UV and SX are connected. We assume here that the entire warm-Compton emission follows the variability of the SX component, that is, that this emission varies with fixed electron temperature and spectral index, contributing SX variability directly into the UVM2 band. This intrinsic disc emission is not predicted by the thin disc equations, but neither is the incomplete thermalization required to form this warm-Compton spectrum. We assume both arise from changes in the disc structure triggered by either the radiation pressure instability and/or atomic opacities (Jiang & Blaes 2020).

We also include the HX reprocessing as well, reverting back to the expected HX scale height of $h_x = 10$, which predicts only low level UV flux variability from HX reprocessing (see Fig. 6). We do not include the reprocessing of the soft-Compton source on the outer disc, as the flat-disc geometry means that the outer disc subtends a very small solid angle to the soft-Compton section of the disc. We refer to this model as **HX10 + WC**. The results of this are shown in Fig. 8, where we find the modelled light curve to have an rms error with respect to the observed of 9×10^{-2}.

We see that this matches the amplitude of longer time-scale variation of UVM2, but again predicts too much fast variability. This can be seen in the CCFs as well. The simulation now matches quite well to the overall amplitude and width of the observed CCF, but has a narrower core, showing that the 4 d time-scale characteristic of the warm-Compton component is too prominent (see the ACF in Fig. 5).

Thus if we assume that the entire component spanning SX to UV energies varies together as a single structure, changing only in normalization – the intrinsic variability of the SX excess – this gives far too much fast variability to the resultant UVM2 curve, although it can match the amplitude and shape of the slower variability.

We can suppress some of the amplitude of variability by assuming the warm Comptonization is not only changing just in normalization but also in spectral index and/or electron temperature, so that the intrinsic soft variations in UVM2 are smaller than those in the SX band. We reduce the amplitude of input variations in UVM2 by an arbitrary factor 2 to see the impact of this effect, yielding Fig. 9. We term this model **HX10 + WC/2**.

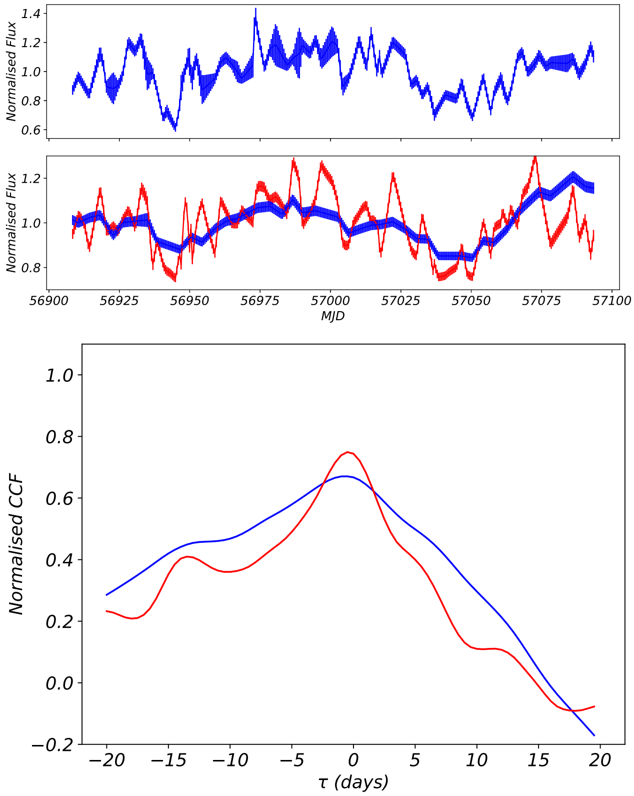

Figure 8. Top panel: HX light curve from *Swift*. Middle panel: blue light curve is observed UVM2 flux. Red shows the simulated light curve from disc reprocessing of hard-illuminating flux, with additional intrinsic soft variability. Bottom panel: CCFs for these light curves, blue for observed CCF, and red for simulated CCF.

This is definitely the best match to the data so far, with an rms error with respect to the data of $6\ \times\ 10^{-2}$. However there is still more fast UVM2 variability predicted than observed, as seen both by comparing the light curves and by the narrow, mildly correlated core of the predicted CCF ($CCF^{max}_{UVM2,HX} = 0.80$.

6 ADDITIONAL REPROCESSING FROM AN INNER BLR/WIND

The data are thus broadly consistent with the majority of the UVM2 variability being *intrinsic* to the warm-Comptonization region. However, the models where this warm-Comptonization region spans between UV and SX, and varies like the SX, results in too much variability in the UV on ~day time-scales, even considering moderate spectral pivoting. Thus, we now explore if part of the UVM2 variability can instead be explained by reprocessing on larger scale structures. Ark 120 clearly has a BLR which subtends a substantial solid angle to the central source, so there should be a UV reprocessed component from this, contributing to the variability, in addition to that arising from an intrinsic disc origin. In NGC 4151 this was the only significant reprocessed contribution to the UV, with no evidence for a disc on smaller scales (MD20).

We first test a model where we assign half of the UVM2 flux to reprocessing in an extended region like the BLR or a wind on its inner edge (see Fig. 2c). This means that the underlying accretion flow model changes, since half of the UVM2 flux is now not connected to direct emission from the disc. A minimal change to the mean `agnsed` model which halves the UV flux while maintaining the X-

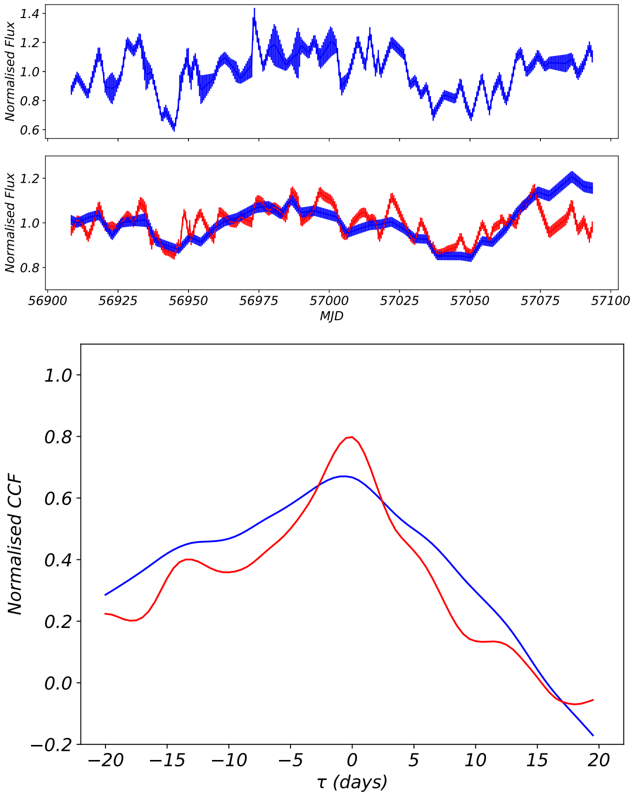

Figure 9. Results for **HX10 + WC/2**. Top panel: HX light curve from *Swift*. Middle panel: blue light curve is observed UVM2 flux. Red shows simulated light curve from disc reprocessing of hard-illuminating flux, with intrinsic soft variations in the UV now suppressed (here by a factor 2) to emulate component pivoting. Bottom panel: CCFs for these light curves, blue for observed CCF, red for simulated CCF.

ray flux can be produced by reducing log (L/L_{Edd}) to -1.45 from the SED mean of -1.31 while increasing R_{hot} from 23.1 to 35 R_g, that is, mainly reducing the SX excess.

Fig. 2(c) then implies that the wind will reprocess both the HX and the warm-Comptonization components. Section 5 has already shown the tension in the warm-Comptonization models for the SX excess, in that the observed SX flux shows much more fast variability than the observed UV flux. Models where the soft Compton varies only in normalization clearly show too much fast variability (Fig. 8). Even assuming that the warm Comptonization changes in spectral index such that its contribution to the UV variability is only half as large as that in the SX shows moderate tension with the level of fast variability in the UV data (Fig. 9). Here, since half of the UV light curve is assumed to be from reprocessing in a more extended region, then the UV variability of directly observed warm Comptonization is diluted, so should give a better match to the data.

We use the hot Compton plus reduced variability warm-Comptonization light curve (**HX10 + WC/2**) as our variable illumination. We assume that all of this is reprocessed in a large-scale region, and give maximal freedom on this by convolving the light curve through an impulse response function (*IRF*). We assume this *IRF* has a Gaussian shape, but truncate this for lags below zero to maintain causality. The UVM2 light curve is then modelled assuming that half of its emission coming from that *IRF* convolution with the HX, and half from the simulated light curve of the pivoting warm-Comptonization model (i.e. the model UV light curve in Fig. 9).

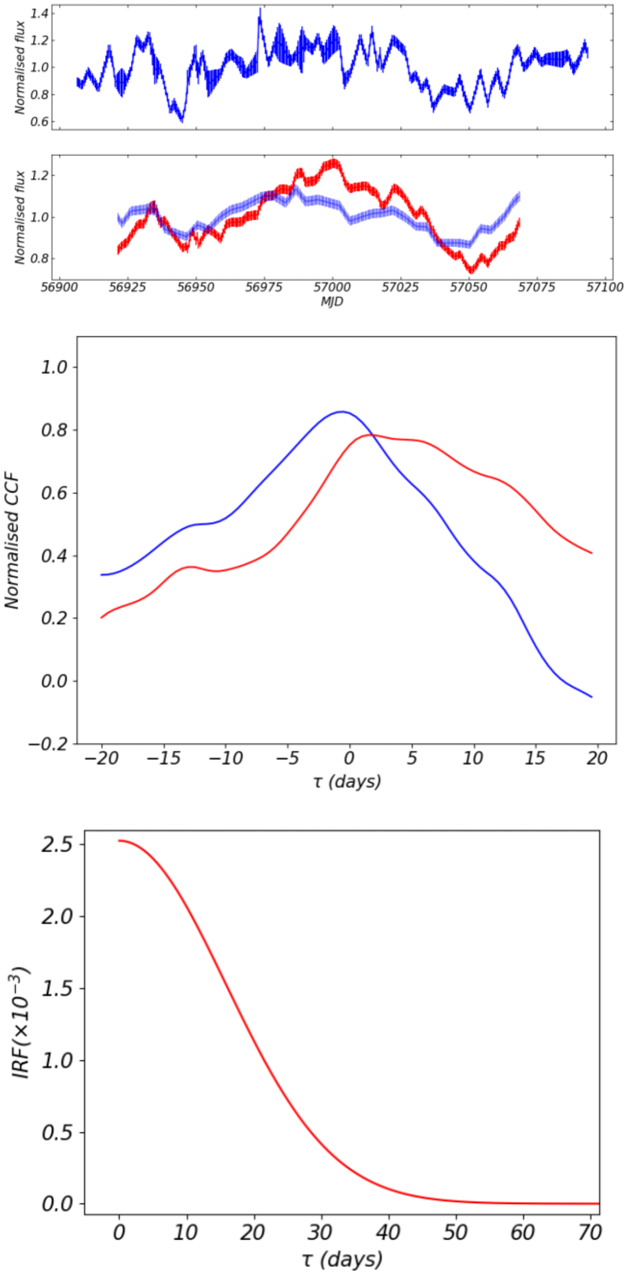

Figure 10. Results of model fit where 50 per cent of the UVM2 flux goes like the results of **HX10 + WC/2** (i.e. like Fig. 9), while the other 50 per cent is produced by a fit impulse response function convolved with the luminosity-weighted sum of the soft- and hard-Compton component curves. The proportions of each Compton component curve fed into the *IRF* convolution are selected such that they match the proportions expected from the SED. Top panel shows observed hard-component light curve. Second panel (blue) shows observed UVM2 curve, while red shows our resultant simulated UVM2 light curve. Third panel shows the CCFs with the usual observed (blue) and simulated (red) colour schemes. Fourth panel shows the best-fitting *IRF* with which half of the driving X-ray flux is convolved.

The parameters describing the *IRF* are then optimized by fitting this modelled UVM2 curve to the data.

Fig. 10 shows the results for the best fit *IRF*. The driving HX light curve (blue) is in the upper panel, while the next panel shows the predicted UVM2 light curve (red) versus that observed (blue). The short-term variability is mostly suppressed, but the predicted

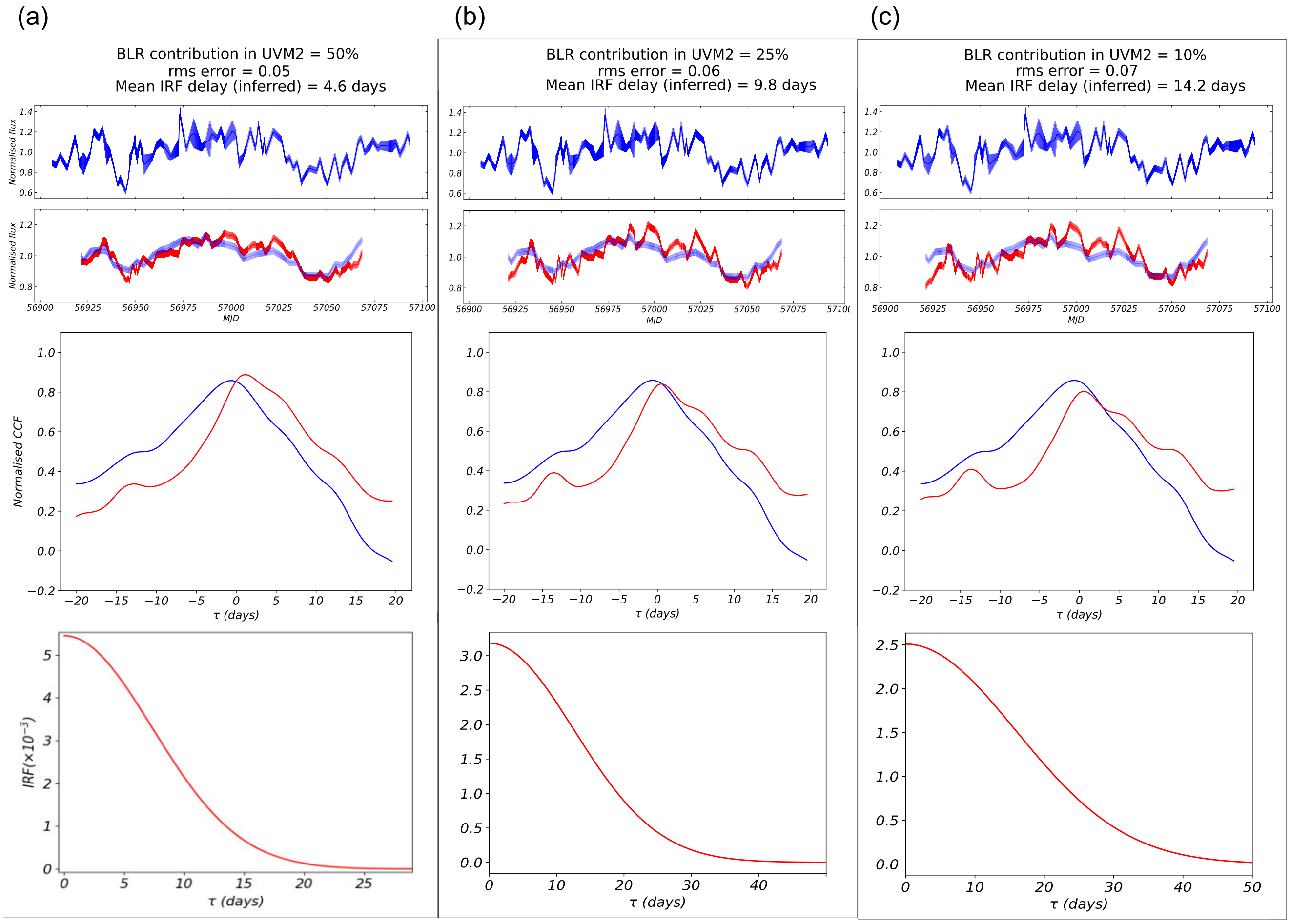

Figure 11. Results of model fits where a percentage of the UVM2 contributions is from the HX (only) being reprocessed through some new impulse response function (*IRF*), (which is allowed to vary in shape such that the simulated light curve best fits the data), while the remained of the UVM2 goes like the results of **HX10 + WC/2** (i.e. like Fig. 9). Top rows show the observed hard-component light curve. Second row panels show observed UVM2 curve in blue, and simulated UVM2 in red. Third row panels shows the CCFs with the usual observed (blue) and simulated (red) colour schemes. Fourth row panels show the best-fitting *IRFs* which result from the UVM2 curve fit.

light curve does not match well to that observed, especially around MJD57000; the overall rms error is quite high, at 0.11. The next panel shows this mismatch more clearly in terms of the CCF between the HX and UVM2 bands, with the predicted UVM2 (red) showing more lagged emission than the real data (blue). This highlights an issue with using the large scale reprocessor as the source of smoothing for the UVM2 light curve. Reprocessing on the light travel time inherently gives a light curve, which is lagged on time-scales similar to the smoothing time-scale. This predicted lag can clearly be seen in the predicted CCF (red), but is not actually present in the observed data (blue). The best-fit reconstructed *IRF* (bottom) peaks at zero lag, but the mean lag is large in order to smooth the X-ray light curve to a level similar to that of the UVM2 data, but this imprints a lag which is not seen in the data.

In Fig. 11(a), we try the same approach, with 50 per cent of the UV variations produced as before by **HX10 + WC/2** but where the *IRF* now reprocesses only the HX Comptonization. This gives the best match so far to the observed long term trends in the UV light curve (with an rms error of 5×10^{-2}). However the CCF still shows the same key discrepancy, in that all these models with a large-scale reprocessor predict a lag on the same time-scale as the smoothing, unlike the data. Further, when more complicated *IRF* forms are tested in the same way as above (e.g. two or three Gaussians instead of one, cf. MD20), these results do not improve; the *IRF* optimizes to the same zero-peaked single Gaussian form to best match the UVM2 curve.

As well as testing a UVM2 light curve composed of 50 per cent BLR-reprocessed X-rays, we can also explore how the behaviour of the model changes when this proportion is reduced. In Fig. 11(b), we show the model results for an IRF optimized to a BLR reprocessing contribution to the UVM2 of 25 per cent, and in Fig. 11(c) we show the case for only 10 per cent. We see that, as the BLR contribution in the UVM2 decreases, we increase the direct component of the warm Comptonization which has too much fast variability for the data.

Existing size estimates for the BLR layers which produce X-ray broad emission lines suggest a minimum radius of 20 ld (Nardini et al 2016, using the iron Kα line FWHM from Chandra/HETG spectra). Meanwhile, Hβ delays with respect to the continuum suggest a size scale for the optical BLR of 40 ld (Peterson & Gaskell 1991). The BLR size scale from our model with only 10 per cent UVM2 BLR contribution is in closest agreement with these estimates. However those predictions are, themselves, model-dependent, with some inferring the size scale from the diffuse continuum from the BLR, while others have it from a wind inwards of the BLR.

7 DISCUSSION AND CONCLUSIONS

Intensive continuum reverberation mapping campaigns, with simultaneous UV and X-ray data, are giving us a new way to probe the accretion flow geometry in AGN. The SED clearly changes with L/L_{Edd}, so we expect that the reverberation signals should also change.

So far, most AGN monitored have been at low L/L_{Edd}. For example, MD20 used the NGC 4151 data to probe the accretion structure at $L/L_{Edd} \sim 0.015$. Here, the source SED peaks at 100 keV, so the bolometric flux is dominated by the HX component, with a weaker peak in the UV. Thus, energetically, the HX reprocessed flux on the disc can produce a large UV variable flux, but this UV reprocessed flux varies too fast unless the disc is truncated below 400 R_g. This used to be very controversial, as X-ray spectral fitting showed a broad residual even after accounting for the (marginally) resolved line seen in the Chandra data for NGC 4151 (e.g. Keck et al. 2015). Most importantly, this appeared to vary as expected from extreme inner disc reverberation (Zoghbi et al. 2012). However, this is now seen as much more likely to be associated with complex and variable X-ray absorption, with no requirement for a relativistic reflection component from the inner disc (Zoghbi et al. 2019). This material is likely to be the inner BLR and/or a wind on the inner edge of the BLR (see also Dehghanian et al. 2019), which likely also produces most of the reverberating UV in this source (MD20).

This is in contrast to the results shown here for Ark 120. This AGN has $L/L_{Edd} \sim 0.05$, and its SED is dominated by a peak in the UV which is larger than the HX component, so the X-rays are not energetically dominant. There is clearly some intrinsic inner disc, probably extending down to $\sim 20 - 30 R_g$ as is probably seen in the moderately broadened reflected spectrum (P18), consistent with the size scale of disc truncation derived in the AGNSED model in order for accretion flow to power the observed X-ray emission. We explore whether the variable UV can be produced by reprocessing of the X-rays in a range of potential geometries and scenarios. First we test whether reprocessing is from an X-ray source of size $\sim 10\ R_g$, but this fails badly, both in under-predicting the amount of UV variability seen, and in reproducing far too much of the fast X-ray variability in the UV light curve (Fig. 6). Instead, we try a much larger scale height for the X-ray source ('lamppost'), at $\sim 100\ R_g$ above the black hole. This gives a larger amplitude of variability from reprocessing, but there is still too much fast variability retained as the light travel times are too short ($\sim$1 d for a 100 R_g scale height and 30 R_g to the inner disc edge: Fig. 7).

Then we allow some fraction of the warm Comptonization to directly emit in the UVM2 bandpass. This already implies that some of the UV variability is intrinsic, rather than simply arising from reprocessing. This increases the amount of variability in the UV, but the warm-Compton component typical variability time-scales are only slightly longer than those of the hard Compton, so this produces far too much fast variability in the predicted UV flux (Fig. 8). Assuming that the warm-Comptonization component variability comes from pivoting rather than a simple change in overall normalization means that the amplitude of this direct component in the UV can be tuned to the data. We find a fairly good match if the UV changes by half the amplitude of the warm-Compton component seen in the SX, but the models still appear to have too much fast variability (Fig. 9). We allow some fraction of the UV variability to be produced by a large-scale reprocessor connected to the BLR or an inner wind. We use a transfer function to give maximal flexibility to the geometry/spectrum of this reprocessor. We assume half of the UV flux arises from this large size scale, while half arises from the accretion flow, and calculate the UV variability arising from disc reprocessed HX (assuming $H_x = 10R_g$) and the direct, but reduced amplitude variable emission from the warm-Compton component. We assume the large-scale reprocessor sees both hot corona and warm Compton. This somewhat overproduces the amount of variability, and also over-predicts the observed lags (Fig. 10). The UV light curves have a typical time-scale of $\sim 10 - 20$ d, but smoothing of the observed HX light curve on these time-scales also implies a similar lag time-scale, which is not present in the data, which is a generic issue for a range of models with a large scale reprocessor (Fig. 11).

We conclude that most of the UV variability must be intrinsic rather than reprocessed. A standard accretion disc cannot vary on these time-scales (see e.g. the discussion in Noda & Done 2018), but the structures required to produce the observed emission do not look like a standard accretion disc but rather are better described by a warm-Comptonization component. However, in the models this spans between the SX and UV as a single component, but the SX excess variability is much faster than the observed UV variability. If this is a single component, then we require that the SX excess is the more variable high-energy tail.

Thus our (lack of) understanding of the UV variability is directly related to our (lack of) understanding of the warm-Comptonization component. This is not seen in the stellar-mass black hole binary systems at the same L/L_{Edd} (see e.g. Done, Gierliński & Kubota 2007), so pointers to the nature of this component may come from the difference between stellar and supermassive black holes. The main change with mass is the temperature of the optically thick accretion material. In the stellar mass systems this is $\sim 10^7$ K, peaking in the X-ray band, while for AGN it reduces to $\sim 10^5$ K, peaking in the UV. Atomic opacities are very important at UV temperatures, but have very little effect at X-ray temperatures. The UV opacity could induce convective turbulence in the disc, and/or power winds which fail and crash back down to the surface, shock heating it to produce all or part of the SX excess (Gardner & Done 2017).

Another difference is in the extent of the radiation pressure dominated section of the disc. This is not the same as the Eddington limit, where the radiation pressure exceeds gravity. Instead, there is an instability which occurs when the radiation pressure exceeds gas pressure inside the disc. The ansatz of a standard Shakura–Sunyaev disc is that the vertically integrated heating rate follows the total pressure, so is $\propto T$ in the gas pressure dominated regime, but $\propto T^4$ in the radiation pressure dominated region. A small fluctuation in temperature leads to a larger fluctuation in pressure in the radiation dominated regime, which leads to a runaway increase in heating. The ratio of radiation to gas pressure goes as $M^{1/4}$ in a Shakura–Sunyaev disc, so is approximately 100 times larger in AGN compared to a BHB at the same Eddington fraction. The standard disc models predict that the inner disc in BHB should also be subject to this instability at $L/L_{Edd} \geq 0.05$, yet the observed BHB discs are extremely stable (see e.g. Gierliński & Done 2004a). This motivates different heating prescriptions, but it remains clear that AGN discs are much more strongly affected by the radiation pressure instability than BHB (see e.g. Grzedzielski et al. 2017).

Jiang & Blaes (2020) include both the UV opacities and radiation magneto-hydrodynamics to capture the full heating rates from magnetic re-connection within the accretion flow. They find that there is some non-linear outcome of atomic opacities coupled to the radiation pressure instability which changes the entire vertical structure of the disc, and that this optically thick flow can vary on the thermal time-scale rather than the much slower viscous time-scales expected in the Shakura–Sunyaev disc.

We speculate that one or more of these processes is responsible for the intrinsic UV variability, on a time-scale which is slow compared to the X-rays. The much faster variability of the SX excess could be produced by shocks from a failed UV line-driven disc wind. The HX have their own even faster variability, but also see the UV and SX as seed photons, so the long term X-ray variability lags the UV on the light travel time, whilst also producing reprocessed UV variability which lags the X-rays on a similar time-scale.

Better monitoring data now exist for Fairall 9, an AGN with similar parameters and a similar SED (Hernandez Santisteban et al. 2020). This will be used to explore these possibilities in subsequent work (Hagen et al., in prep.).

ACKNOWLEDGEMENTS

RDM acknowledges the support of a Science and Technology Facilities Council (STFC) studentship through grant number ST/N50404X/1. CD acknowledges the STFC through grant number ST/T000244/1 for support, and multiple conversations about the Fairall 9 data with Scott Hagen, and Rick Edelson.

DATA AVAILABILITY

X-ray and UV data underlying this article are available at NASA's HEASARC archive (https://heasarc.gsfc.nasa.gov/cgi-bin/W3Browse/w3browse.pl). Access to the reprocessing code is available on request from CD (chris.done@durham.ac.uk).

REFERENCES

Boissay R., Ricci C., Paltani S., 2016, A&A, 588, 70
Buisson D. J. K., Lohfink A. M., Alston W. N., Fabian A. C., 2017, MNRAS, 464, 3194
Cackett E., Chiang C.-Y., McHardy I., Edelson R., Goad M. R., Horne K., Korista K. T., 2018, ApJ, 857, L53
Cackett E., Zoghbi A., Otho U., 2022, ApJ, 925, L29
Cardelli J. A., Clayton G. C., Mathis J. S., 1989, ApJ, 345, L245
Crummy J., Fabian A. C., Gallo L., Ross R. R., 2006, MNRAS, 365, 1067
Davis S. W., Woo J.-H., Blaes O.M, 2007, ApJ, 668, L682
Dehghanian M. et al., 2019, ApJL, 882, L30
Done C., Gierliński M., Kubota A., 2007, A&ARv, 15, 1
Done C., Davis S. W., Jin C., Blaes O., Ward M., 2012, MNRAS, 420, 1848
Edelson R. et al., 2015, ApJ, 806, L129
Edelson R. et al., 2017, ApJ, 840, L41
Edelson R. et al., 2019, ApJ, 870, L123
Gardner E., Done C., 2017, MNRAS, 470, 3591
Gierliński M., Done C., 2004a, MNRAS, 347, 885
Gliozzi M., Papadakis I. E., Grupe D., Brinkmann W. P., Rath C., 2017, MNRAS, 464, 3955
Grzedzielski M., Janiuk A., Czerny B., Wu Q., 2017, A&A, 603, 110
Hernandez Santisteban J. V., Horne K., 2020, MNRAS, 498, 5399
Jiang Y.-F., Blaes O., 2020, ApJ, 900, L1
Jin C., Ward M., Done C., Gelbord J., 2012, MNRAS, 420, 1825
Kammoun E. S., Papadakis I. E., Dov̌ciak M., 2019, ApJ, 879, L24
Kammoun E. S., Papadakis I. E., Dov̌ciak M., 2021, MNRAS, 503, 4163
Kara E., Fabian A. C., Cackett E. M., Steiner J. F., Uttley P., Wilkins D. R., Zoghbi A., 2013, MNRAS, 428, 2795
Kara E. et al., 2021, ApJ, 922, L151
Keck M. L. et al., 2015, ApJ, 806, L149
Kelly B. C., Becker A. C., Sobolewska M., Sieminginowska A., Uttley P., 2014, ApJ, 788, 33
Korista K. T., Goad M. R., 2001, ApJ, 553, L695
Korista K. T., Goad M. R., 2019, MNRAS, 489, 5284
Kubota A., Done C., 2018, MNRAS, 480, 1247
Lawther D., Goad M. R., Korista K. T., Ulrich O., Vestergaard M., 2018, MNRAS, 481, 533
Lobban A. P., Porquet D., Reeves J. N., Markowitz A., Nardini E., Grosso N., 2018, MNRAS, 474, 3237
Lobban A. P. et al., 2020, MNRAS, 494, 1165
Lusso E., Risaliti G., 2017, A&A, 602, 79
Mahmoud R. D., Done C., 2018, MNRAS, 473, 2084
Mahmoud R. D., Done C., 2020, MNRAS, 491, 5126
Matt G. et al., 2014, MNRAS, 439, 3016
Mehdipour M. et al., 2011, A&A, 534, 39
Mehdipour M. et al., 2015, A&A, 575, 22
Mehdipour M. et al., 2016, A&A, 588, 139
Miller J. M. et al., 2018, ApJ, 865, L97
Nardini E., Porquet D., Reeves J. N., Braito V., Lobban A., Matt G., 2016, ApJ, 832, L45
Noda H., Done C., 2018, MNRAS, 480, 3898
Noda H., Minezaki T., Watanabe M., 2016, ApJ, 828, L2
Patrick A. R., Reeves J. N., Lobban A. P., Porquet D., Markowitz A. G., 2011, MNRAS, 416, 2725
Peterson B. M., Gaskell C. M., 1991, ApJ, 368, L152
Petrucci P. O., Ursini F., De Rosa A., Bianchi S., Cappi M., Matt G., Dadina M., Malzac J., 2018, A&A, 611, 59
Porquet D., Reeves J. N., O'Brien P., Brinkmann W., 2004, A&A, 422, 85
Porquet D. et al., 2018, A&A, 609, 42
Porquet D., Reeves J. N., Grosso N., Braito V., Lobban A., 2021, A&A, 654, 89
Ruan J. J., Anderson S. F., Eracleous M., Green P. J., Haggard D., MacLeod C. L., Runnie J. C., Sobolewska M. A., 2019, ApJ, 883, 76
Uttley P., Cackett E. M., Fabian A. C., Kara E., Wilkins D. R., 2014, A&A Rev., 22, 72
Walton D. J. et al., 2013, ApJ, 779, L148
Wilms J., Allen A., McCray R., 2000, ApJ, 542, L914
Xie Y., Li A., Hao L., 2016, ApJS, 228, 1
Zoghbi A., Fabian A. C., Reynolds C. S., Cackett E. M., 2012, MNRAS, 422, 129
Zoghbi A., Miller J., Cackett E., 2019, ApJ, 884, L26

This paper has been typeset from a TEX/LATEX file prepared by the author.